Schweizerische Eidgenossenschaft
Confédération suisse
Confederazione Svizzera
Confederaziun svizra

Eidgenössisches Departement für
Umwelt, Verkehr, Energie und Kommunikation UVEK

Bundesamt für Energie BFE

Modeling of energy conversion processes at the microscale with application to PEFCs.

Final Report

Author and Co-Authors	N. I. Prasianakis, F. N. Büchi, J. Mantzaras
Institution / Company	Combustion fundamentals Group, Paul Scherrer Institut (PSI)
Address	Paul Scherrer Institut (PSI), Villigen CH-5232
Telephone, E-mail, Homepage	056-3104046, ioannis.mantzaras@psi.ch , cfg.web.psi.ch
Project- / Contract Number	154001 / 103078
Duration of the Project (from – to)	
Date	04.12.2012

ABSTRACT

Main goal of the project was the development of an advanced numerical tool capable of modeling key microscale processes occurring in both thermochemical and electrochemical conversion systems. A particular objective was to apply the new model in a PEFC and compare the predictions with measurements of permeabilities and diffusivities inside the gas diffusion layer (GDL). The method of approach involved:

a) developing a new mesoscale Lattice Boltzmann model for: multi-species, non-isothermal, reacting, complex three-dimensional geometry flows, and

b) carrying out permeability and diffusivity experiments in a model PEFC.

The main results are summarized below:

- Thermal-multicomponent LB model derivation 2D and 3D, and validations in a large number of benchmark flows.
- Simulation of 3D porous media flows with application to PEFCs.
- Validation of complex geometry algorithm in 2D and 3D against experiments as well as against other CFD numerical tools.
- Study and characterization of the GDL properties, using in-situ X-ray tomography under normal operational conditions (saturation dependent permeability and diffusivity).
- Simulation of bulk chemical reactions.

Table of contents

1. Motivation and Project Tasks

One of the most important scientific challenges of modern time is the efficient generation of electrical energy. The optimization and development of advanced energy conversion systems (converting chemical to electrical energy) is based on the understanding of the underlying thermochemical and electrochemical processes. Such systems can include complex structural components such as catalytic microreactors in the case of turbines for energy generation, gas diffusion layers (GDL's) in the case of polymer electrolyte fuel cells (PEMC), or even porous burners that can serve as combustion chambers.

Recent advances in computer technology along with the improvement of computer algorithms, allows the simulation of more realistic and complex physical systems. Computer clusters that contain thousands of processors are nowadays easily accessible. In terms of modeling, the description of physical systems and the resulting scientific achievements feature an exponential growth.

The project goal was to develop advanced numerical tools capable of modeling key microscale processes occurring in both thermochemical and electrochemical conversion systems. In such systems, complex phenomena are acting at different time scales (from microseconds for the chemical time scales to seconds for thermal conduction in the solid) and length scales (from microns in the porous gap to centimeters in fuel cell stacks). Moreover, the associated small sizes (porous electrode structures in fuel cells, porous catalytic layers in combustion systems, etc.) necessitate the construction of specialized models since classical continuum approaches are not applicable at very small scales. The physicochemical processes at the micro- and meso-scale are not well understood, but they ultimately control the performance of such systems. Key to understanding and optimizing the efficiency and durability of energy conversion units is, from a design point of view (materials development being the other main intrinsic aspect), the combination of **advanced modeling (fluid dynamics)** and sophisticated **experimental diagnostics (X-ray micro tomography)**. A particular objective was to apply the new model in a Polymer Electrolyte Fuel Cell (PEMC) and compare the predictions with measurements of permeabilities and diffusivities inside the gas diffusion layer.

The specific goals (tasks) set in the project were the following:

Task 1:	Develop a new 2D thermal mixture LB model for complex geometry.
Task 2:	Add bulk chemical reactions and catalytic surface reactions. This will allow the simulation of reactive flows through catalytic channels.
Task 3:	Extend the energy conserving mixture model to three dimensions (3D) with inclusion of chemical reactions.
Task 4:	Develop complex geometry boundary conditions for the 3D model.
Task 5	Perform digital 3D reconstruction of selected GDL materials using X-ray micro tomography. Simulation of flow and comparison with experimental results using the 2D LB model.
Task 6:	Simulation of flow and comparison with experimental results using a full 3D real porous geometry.

2. Thermal mixture Lattice Boltzmann model development (Tasks 1, 3)

The major theoretical result was the development of an advanced lattice Boltzmann model (LB) capable of simulating simultaneously mass and heat transport processes in mixture flows. Starting point of the development was the experience and expertise: a) in single component energy conserving modeling (Dr. N. Prasianakis [1-5]), and b) in multi-component isothermal modeling (Drs. I. Mantzaras and S. Arcidiacono [6-9]), as illustrated in Fig. 1.

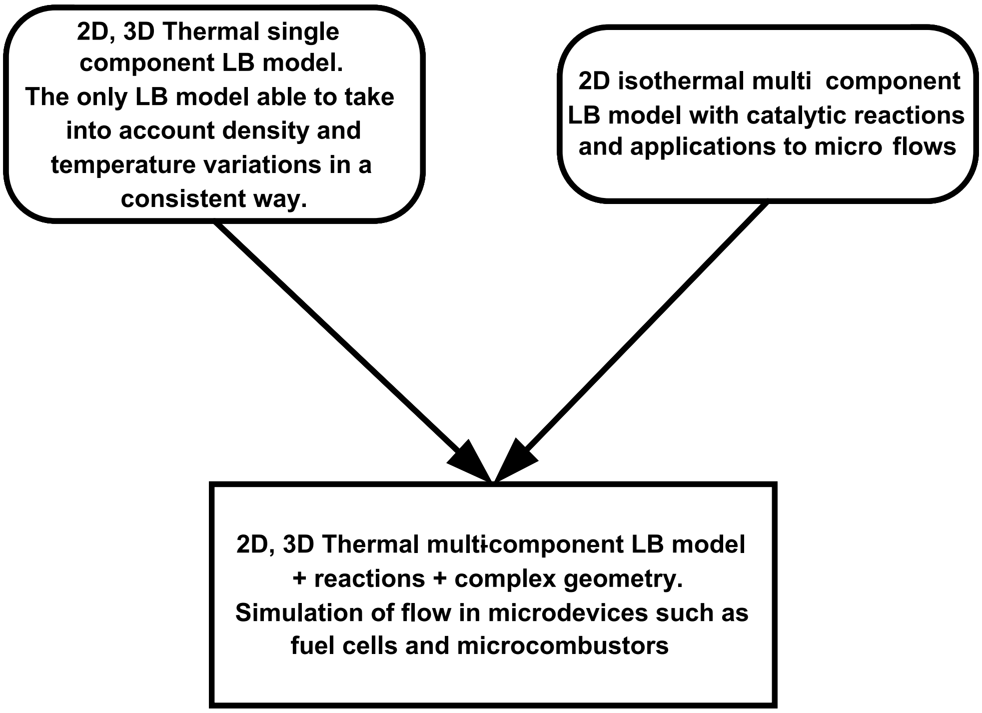

Figure 1: Proposed pathway for modeling activity at PSI/CFG. Knowledge on thermal LB models (energy conserving) has been combined with isothermal multi-component model knowledge for simulation of practical applications in two and three dimensions (flow in SOFCs-PEFCs, microreactors).

The suggested pathway required the derivation and theoretical analysis of new models, since it was not possible to simply combine existing ones. To this purpose, new algorithms and new models (equilibrium functions, correction terms, time-space discretization) have been created from first principles.

The resulting model is presented in Ref. [10] as well as in the Appendix. An asymptotic analysis followed the derivation of the LB model and allowed assessment of its macroscopic behavior. Deviation terms have been identified for the two-dimensional (2D) as well as the three-dimensional equivalent model (3D). Specifically designed correction terms were added, in order to guarantee that the model recovers the desired macroscopic equations. Simulation of mixture flows under the presence of temperature gradients is now possible. The Prandtl number, the Schmidt number and therefore the Lewis number are now adjustable. For validation purposes several benchmark flow setups have been used. The agreement between the LB algorithm and the analytic solutions or other numerical CFD solutions is excellent.

• 2.1. Mixing (Mass diffusivity)

The mixing process of a binary mixture (with a molecular mass ratio $M_A/M_B = 4$) has been simulated using the new thermal mixture model. The initial concentrations on the left side: are 65% Component A and 35% Component B. On the right side, the concentration is 35% Component A and 65% Component B. The two regions are brought in contact and diffusion starts at t = 0. For this specific problem, there exists an analytic solution which is also plotted in Fig. 2 along with the LB simulations.

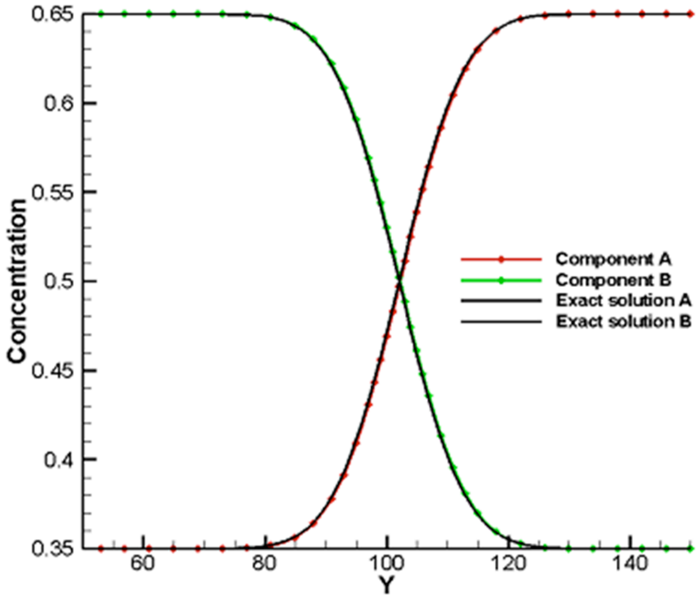

Figure 2. Binary diffusion of a two-component mixture: comparison of LB predictions with analytic solution. Symbols depict the simulation results; solid lines depict the analytic solution (results are shown at a given time step of the transient process).

• 2.2. Viscosity and thermal diffusivity

The thermal mixture model was tested in a Couette flow and in the case of heat diffusion over a semi-infinite plane. The Couette flow is established between two parallel plates, when one plate moves with a specified velocity with respect to the other plate. The top wall has a velocity in lattice Boltzmann units equal to u_{top}=0.2, and the bottom wall is stationary (see Fig. 3).

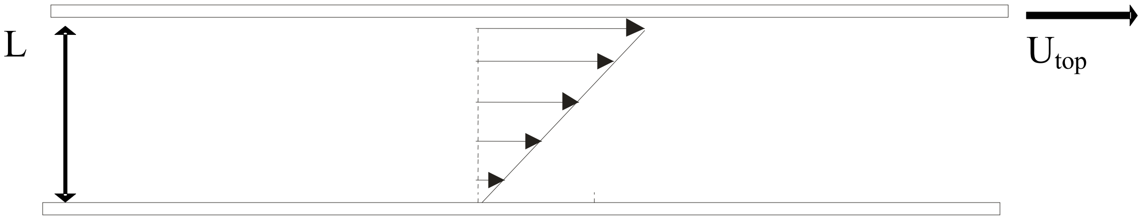

Figure 3. Schematic of the Couette flow setup. The flow is included between two parallel plates (top-bottom), which are moving with different velocities. On the left and right side of the domain, periodic boundary conditions are applied.

Simulation results are shown in Fig. 4a, at two different time instances as well as at the final steady state. Symbols depict the simulation results, while the solid black lines stand for the analytic solution. This benchmark allows for testing the viscosity of the numerical model.

Similar to the Couette flow, the heat diffusion in a semi infinite plate allows checking for the thermal conductivity and heat diffusivity of the model. The left boundary of the 2D simulation domain is kept at a temperature T_{wall} while the rest of the domain is kept at a lower temperature T_∞. Heat diffusion takes place and the results are plotted in Fig. 4b. Again, symbols depict the simulation results, while the solid black lines stand for the analytic solution.

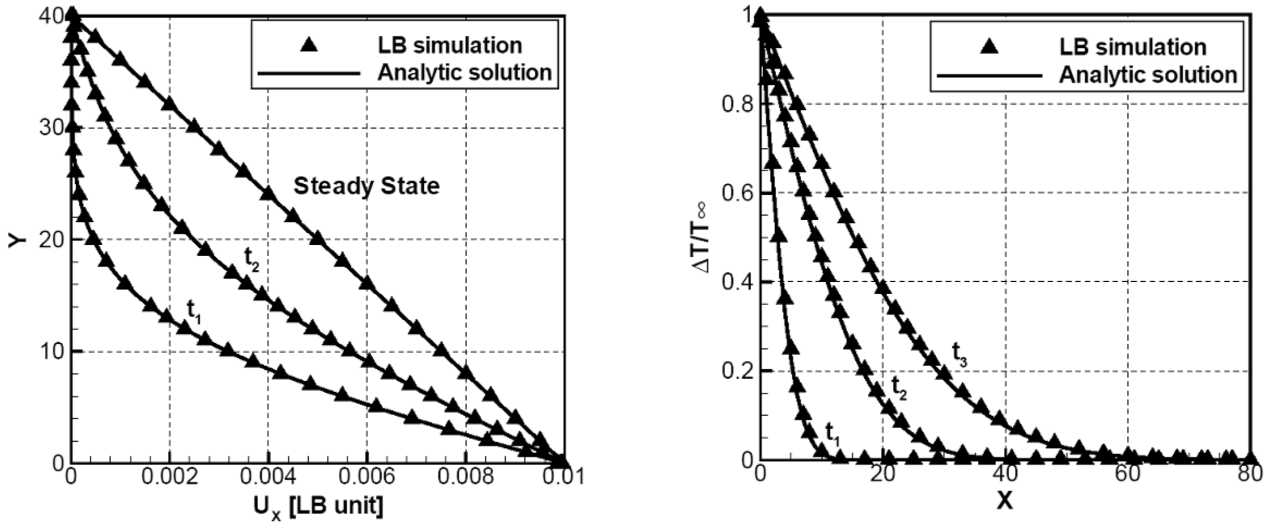

(a) (b)

Figure 4. Comparison of simulation results with analytic solutions for the Couette flow (a), and for the heat diffusion in a semi infinite plate (b). Symbols are the LB simulation results, and solid lines are the analytic solutions. Time instances for the Couette flow: t_1=1000, t_2=3000, for the heat diffusion case: t_1=1.000, t_2=10.000, t_3=30.000.

2.3. Mixing under the presence of temperature gradients

In the case of mixing under the presence of temperature gradients, the comparison is against a finite difference based numerical tool. Mixing of two species under the presence of temperature gradients is studied. A 2D domain filled with a mixture of two species A and B is considered. The molecular weight of species A is M_A = 1g/mol and of species B is M_B = 4g/mol. The size of the domain is 0.4 m, along the x-direction and infinitely long in the y-direction. The domain is divided in two regions, left and right, which contain mixtures of species A and B at equilibrium, held at different temperatures and compositions. The mole fractions at the left side are X_A = 51% and X_B = 49% at a temperature of 360K. The right region has a composition of X_A = 49% and X_B = 51% and is held at a temperature of 840K. At time t = 0 the interface that separates the two regions is removed and due to the existence of concentration and temperature gradients, mixing and heat transfer takes place at the same time. The changes in composition affect the heat transfer throughout the domain and, at the same time, the temperature changes affect the diffusion of species. Comparison between the LB algorithm and the finite difference based tool is shown for two different time instances t=1s and t=30s in Fig. 5a,b.

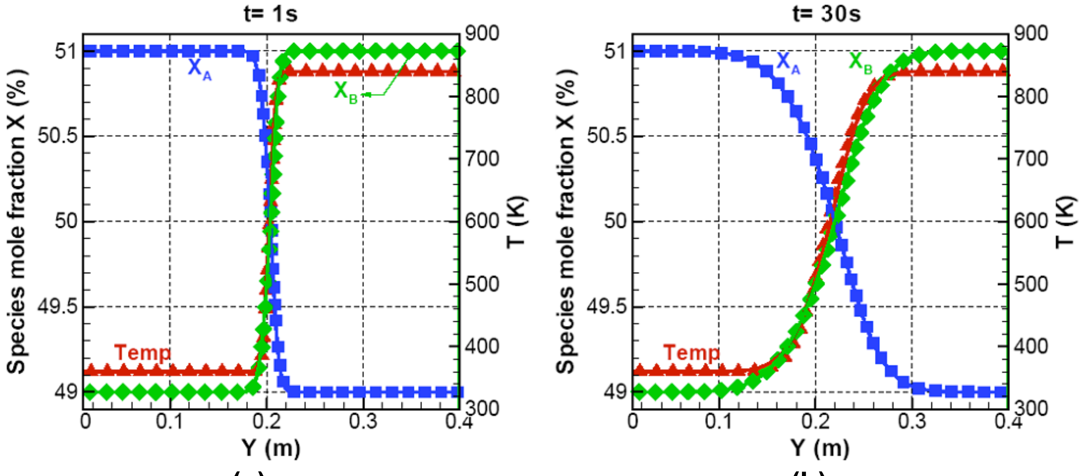

(a) (b)

Figure 5. Mixing under the presence of temperature gradients: Comparison of LB simulation results with numerical CFD prediction at different time instances, (a) t = 1 s and (b) t = 30 s. (The red line and triangles denote the temperature, blue line and squares the mole fraction of gas A, and green line and diamonds the mole fraction of B.)

2.4. Opposed jet flow (large velocity, concentration and temperature gradients)

The final benchmark that compelted the validation studies of the model was the opposed jet flow setup. Two opposite jets with different species composition, momentum and temperature flow against each other. The comparison is done using the OPPDIF algorithm, a numerical tool developed at Sandia National Laboratory, USA [11]. The flow setup is depicted in Fig. 6a. A mixture of H_2O and O_2 enters from the left side of the domain with mole fraction X_{H2O}=10%, X_{O2}=90%, velocity U_{Left}=0.61m/s, and temperature T_{Left}=300 K. A mixture with the same species but at different composition, temperature and velocity enters from the right side of the domain with X_{H2O}=90%, X_{O2}=10% , velocity U_{Right}= -1.04m/s, and temperature T_{Right}=300 K. The mixture exits from the top end bottom boundaries. Strong velocity, concentration and temperature gradients exist in the domain. The agreement between the LB result and the OPPDIF algorithm is excellent and is plotted in Fig 6b.

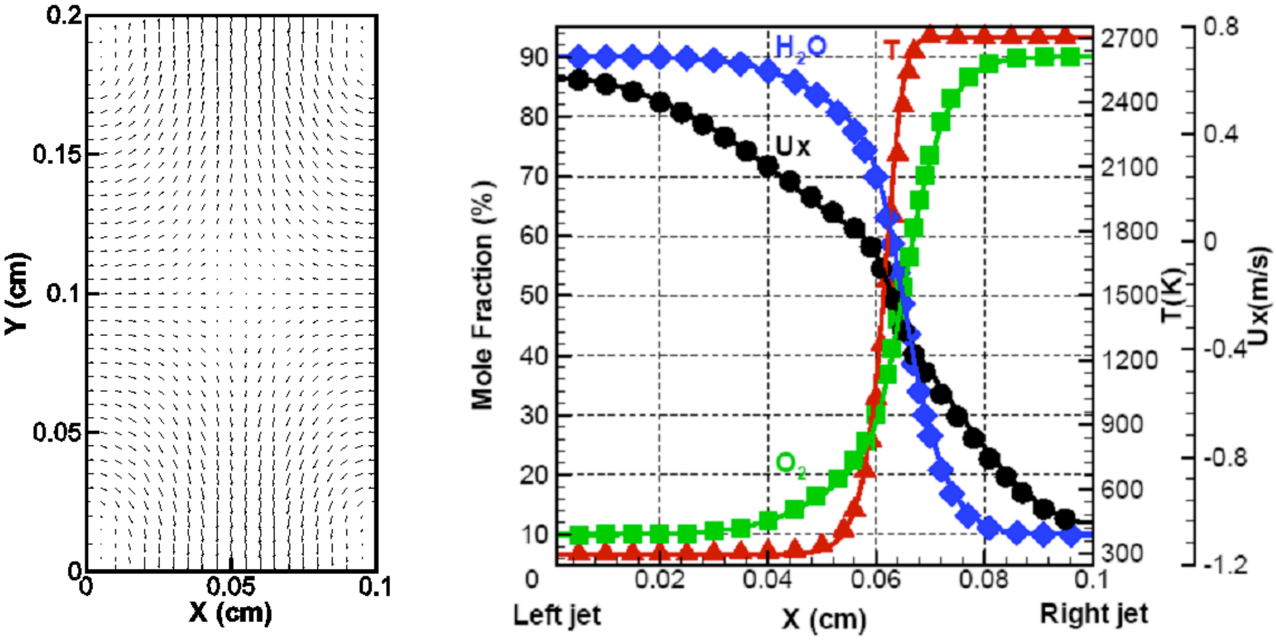

(a)

(b)

Figure 6. The simulation domain is illustrated on the left. Two opposite jets enter from the left and right sides and exit from the bottom and top boundaries. Comparison between LB simulation results (symbols) and OPPDIF algorithm (solid lines), at the centerline (Y=0.1cm) is depicted on the right side. (Red line and triangles represent temperature, blue line and diamonds represent H_2O, green line and squares represent O_2, black line and circles represent magnitude of velocity in the X direction.)

3 Thermal mixture model with chemical reactions: Hydrogen combustion simulations (Task 2)

The model of Ref. [1-4] has been extended to address a wide range of combustion phenomena and reactive flows. On top of the thermal model, a model for the advection and diffusion of species equations has been introduced. Moreover, a specifically designed term has been added at the level of the kinetic equation to account for the heat release of reactions in the bulk.

The resulting model is a state-of-the art approach with unique features. Reactive flows with significant temperature and density variations can be simulated without loss of numerical stability and most importantly with very good accuracy. The mass conservation equations for the chemical species have been designed in such a way that compressibility effects can be also taken into account. **For that purpose, a new scheme for solving the advection-diffusion equations of chemical species has been proposed.** The advantage of the new advection-diffusion scheme is shown in Fig. 7.1, where the species mass fractions along the channel walls are plotted (For test case 1, Uin=0.85m/s). More details about the model can be found in Ref. [12].

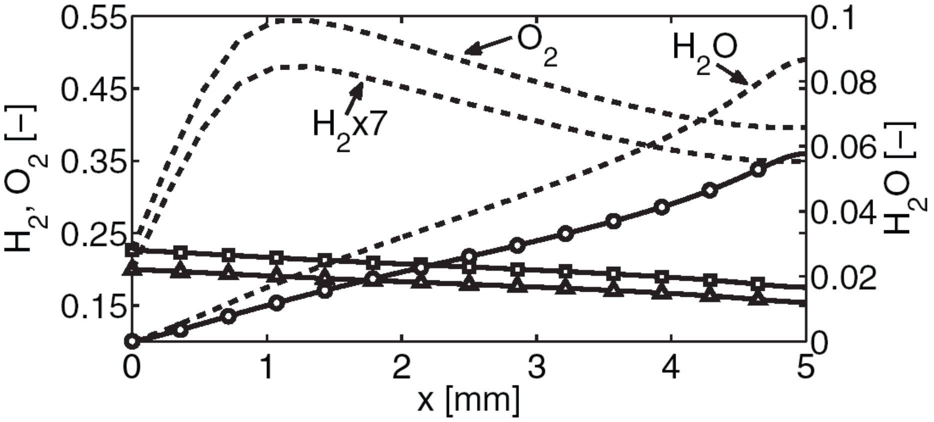

Figure 7.1. Species mass fractions along the channel walls predicted by standard advection-diffusion approach are compared to those recovered by the proposed model (solid lines). Symbols are the reference solution for test case 1 (circles H_2O, squares O_2, triangles H_2).

The effectiveness of the proposed approach has been proven by simulating combustion of hydrogen/air reactive mixtures in a mesoscale channel, and by further validating against reference numerical solution. The numerical CFD tool that has been used is the commercial CFD solver FLUENT [13]. For the specific numerical benchmark, the stoichiometric combustion of a hydrogen/air reactive mixture has been considered.

The simulation domain is confined between two parallel horizontal plates with a fixed length-to-height aspect ratio, L/h=2.5 and length L= 5 mm. This domain is usually referred to as mesochannel [14]. Ignition of the reactive mixture is produced and sustained by heated walls. For fixed values of the channel height h and the wall temperature, different types of flames are observed, as function of the inlet velocity Uin. Constant temperature Tin =300 K is prescribed at the inflow and a well premixed stoichiometric H_2-air mixture enters from the left side (inlet). The global reaction $H_2 + 1/2O_2 \rightarrow H_2O$ with kinetics by Marinov et al. [16] was employed. For the results presented in this section, the inlet velocity is set to Uin =0.85 m/s in ***test case 1*** and Uin =0.48 m/s in ***test case 2***.

For the test case 1, the inlet velocity does not allow full combustion of the mixture. Nevertheless, reactions take place and temperature of the mixture gradually increases following the conversion of H_2 and O_2 to H_2O. Simulation results are compared with the results of FLUENT solver in Fig. 7.2. For test case 2, a closed symmetric flame is anchored at the vicinity of the inlet and fully converts the fuel within the channel. Simulation results are compared in Fig. 7.3, where the mixture density, x-velocity component, mixture temperature and H_2 mass fraction profiles are plotted along the horizontal plane of symmetry. Solid lines and symbols represent the LB and the reference CFD solutions respectively. Finally, in Fig. 7.4 the mass fractions of H_2O and O_2 for both cases are plotted side-by-side. In all the plots an excellent agreement is observed.

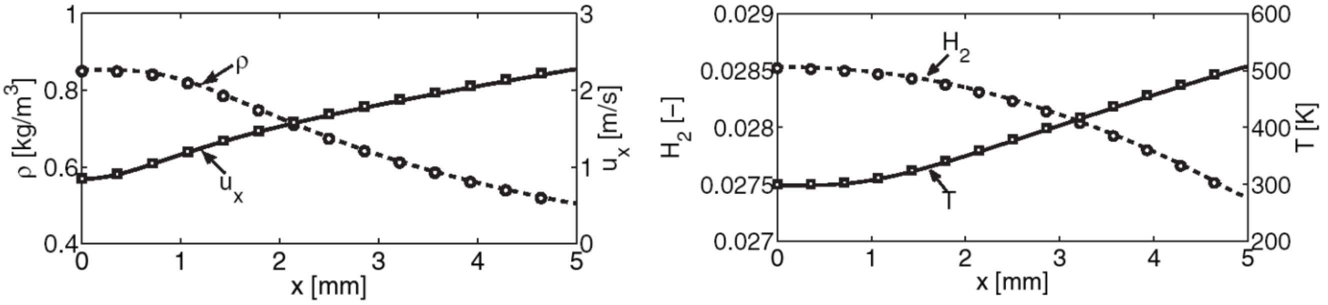

(a) (b)

Figure 7.2. Test Case 1(Uin=0.85m/s): (a) mixture density and x-velocity component along the horizontal plane of symmetry. Solid lines and symbols represent the LB and the reference CFD solutions, respectively. (b) mixture temperature and H_2 mass fraction along the horizontal plane of symmetry. Solid lines and symbols represent the LB and the reference solutions, respectively.

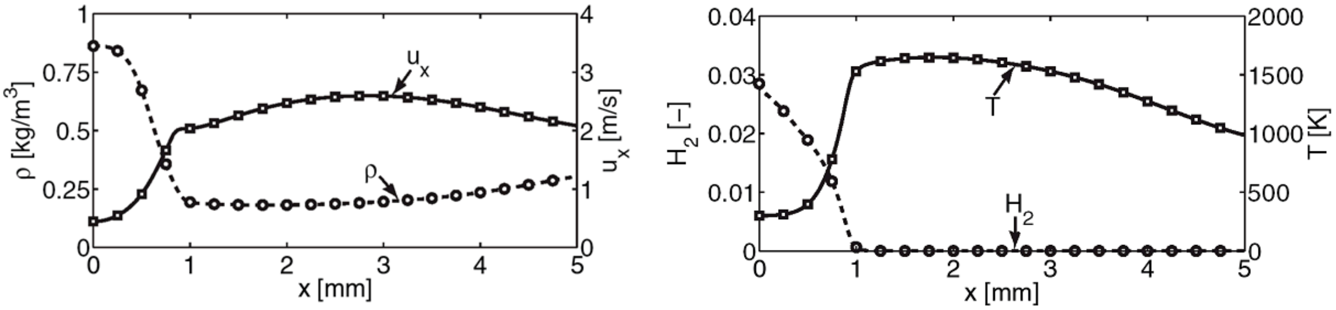

(a) (b)

Figure 7.3. Test Case 2(Uin=0.48m/s): (a) mixture density and x-velocity component along the horizontal plane of symmetry. Solid lines and symbols represent the LB and the reference CFD solutions, respectively. (b) mixture temperature and H_2 mass fraction along the horizontal plane of symmetry. Solid lines and symbols represent the LB and the reference solutions, respectively.

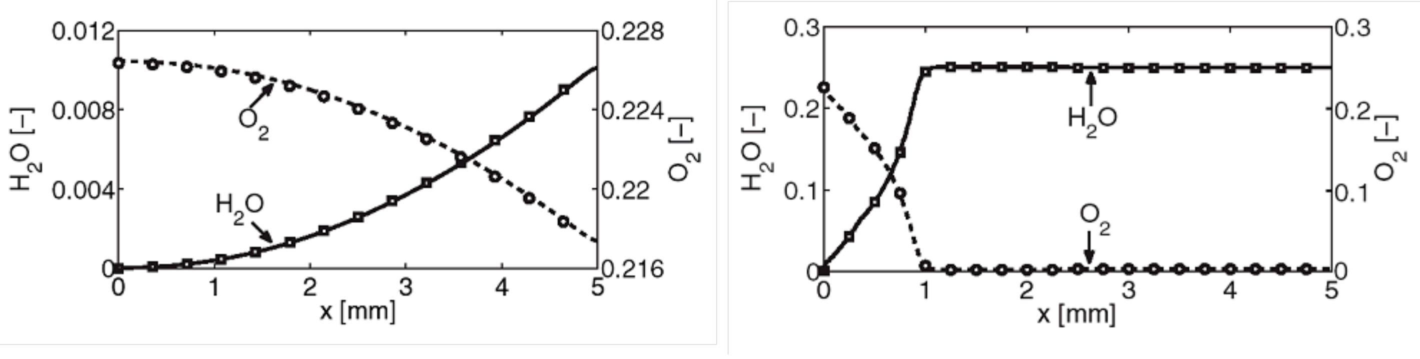

(a) (b)

Figure 7.4. Both test Cases (a) mass fraction of H_2O and O_2 along the horizontal plane of symmetry, for Uin=0.85m/s (b) mass fraction of H_2O and O_2 along the horizontal plane of symmetry for Uin=0.48m/s. Solid lines and symbols represent the LB and the reference CFD solutions, respectively.

4. 3D LBM complex geometry accuracy and validation (Tasks 4-5)

4.1. Accuracy study and Boundary conditions

The accuracy of the single component D2Q9 and D3Q27, in-house developed algorithm is examined. All LB models available in the literature result in an accuracy that depends on the grid resolution and on the boundary condition implementation method. Moreover, there exists the so-called “viscosity dependency” of the result which constrains the application of the method to a limited number of cases. As an example, the Poiseuille flow between two parallel plates (2D and 3D) is considered (Fig. 8). In Fig. 9a, the error compared to the analytic solution of the velocity profile, versus the viscosity of the code (LB units) is plotted. Three different implementations have been considered:

(a) Simple bounce back boundary condition (BB) and the LB model found in Ref. [17] (Standard implementation; blue dashed lines)
(b) Half-way bounce back (HBB) and the LB model found in Ref. [17] (Blue solid lines)
(c) Half-way bounce back (HBB) and our single component LB model Ref.[3] (Black solid lines)

It can be seen, that for implementations (**b**) and (**c**), for small viscosity values (in LB units, which correspond to low Knudsen numbers and macro-fluidic flow), the computational error is 1% for a channel width discretization of 9 nodes (H=9).

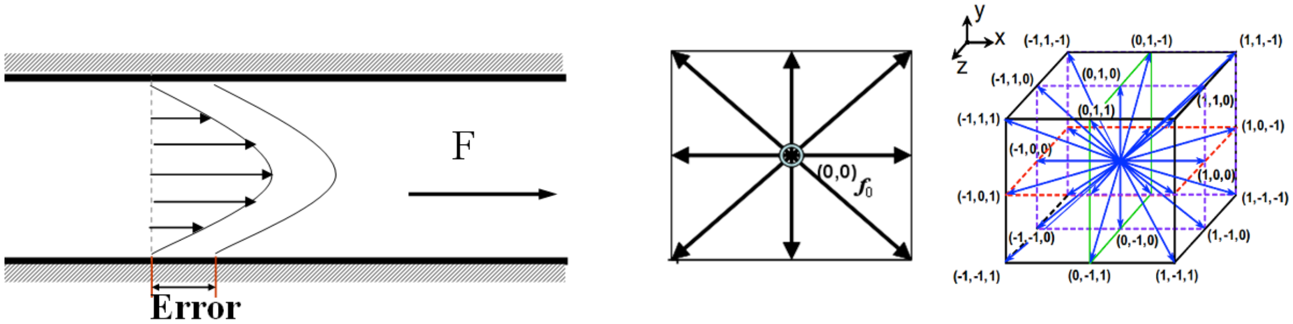

(a) (b) (c)

Figure 8. (a) The error source of the Poiseuille flow in LB algorithms, stems from the boundary condition discretization; (b) D2Q9 lattice; (c) D3Q27 lattice.

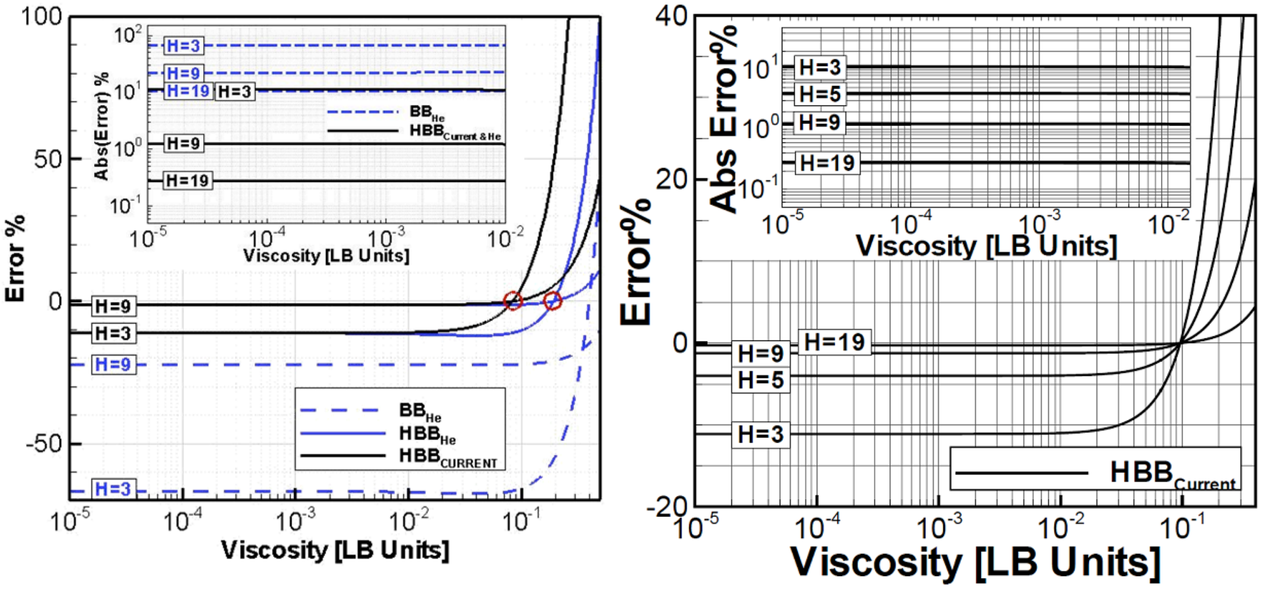

(a) (b)

Figure 9. (a) Accuracy of 2D Poiseuille flow regarding different boundary condition implementation methods, resolution (H=[3,9,19]) and viscosity (LB units); (b)Accuracy of 3D Poiseuille flow between two parallel plates. Solutions for different grid resolution (H=[3, 5, 9,19]) versus the viscosity (LB units) are plotted.

Similar results are obtained also for the 3D case (Fig. 9b) by using our D3Q27 implementation. For our subsequent porous media simulations, we take care that the minimum porous width is not less than H=5. Implementation (**a**) results in large errors and shall not be used for porous media flows. It should be noted that the aforementioned methods are only suitable for macro-flow calculation. For the micro-flow regime (viscosity > 0.1 in LB units) the diffusive boundary condition has to be considered (Ref. [18]).

4.2. Simulation of flow through complex geometries using the 3D LBM model. (Task 5,6)

A 3D reconstructed sample of carbon fiber paper Toray TGPH-060 with 20% PTFE wet proof treatment is used to make a first calculation using our 3D LBM model (Fig. 10ab). The sample's dimension is 370 x 150 x 131 micrometers, and a uniform forcing field is applied between the inlet and outlet and drives the flow. Periodic boundary conditions for all other directions are implemented.

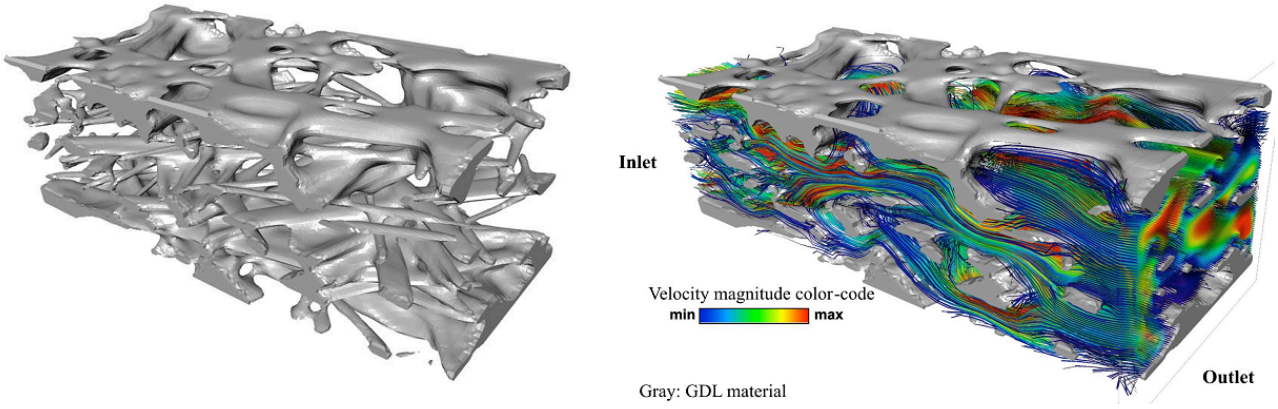

(a) **(b)**

Figure 10. (a) 3D reconstructed GDL sample, size: 370 x 150 x 131 micrometers; (b) Streamlines of the flow through GDL sample.

In Fig. 10b, the streamlines (velocity field) of the resulting flow inside the GDL fluid domain are depicted. Permeability and effective diffusivity values can be extracted directly from the flow field.

4.3. Validation of 3D LBM against Stokes Solver.

For validation purposes, we compare the simulations of the flow through the structures of Fig. 11a with a computational tool developed at the Fraunhofer Institut (Stokes equation Solver) and with experimental results obtained at PSI.

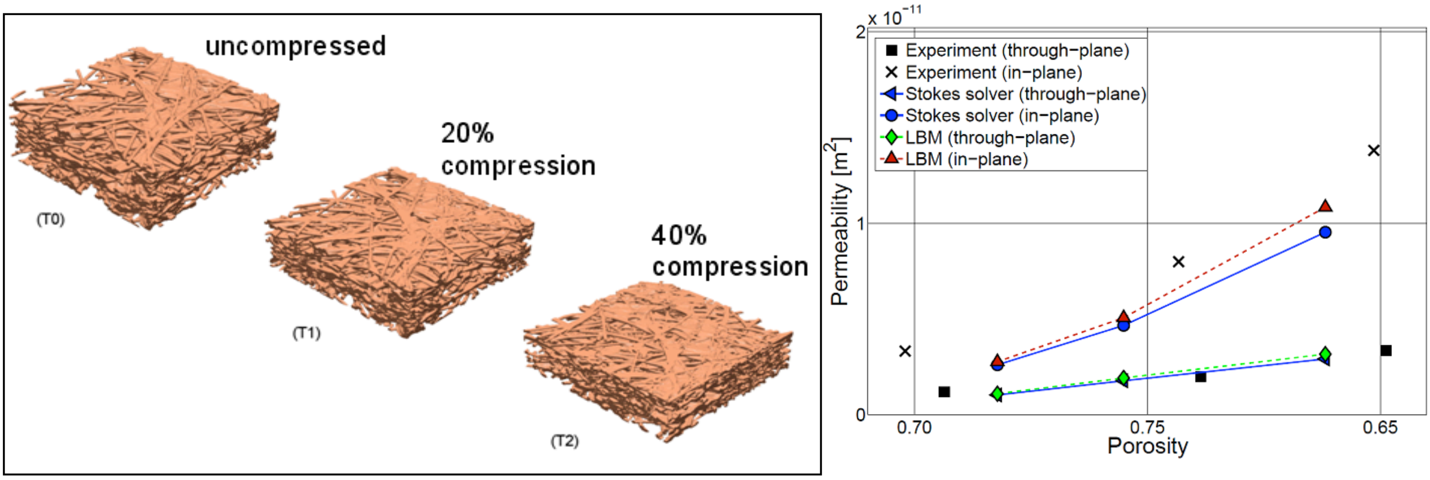

(a) **(b)**

Figure 11. (a) 3D reconstructed structures for different compression rates, using X-Ray Tomographic Microscopy. (F. Büchi, Beamline SLS); (b) Permeability results for in-plane and through-plane cases, at different compression rates (0%, 20% and 40%). Experiments, Stokes-solver and LB results are compared.

The resulting permeability is compared in Fig. 11b for 3 samples at different compression rates. The permeability changes when the GDL material is compressed, due to the resulting change in porosity. This compression occurs during the assembly of the fuel cell. All results are in excellent agreement for the through-plane case.

5. Study of the GDL properties using in-situ X-ray tomography pictures under normal operational conditions (Task 6)

One of the project goals was the simulation of flow through the gass diffusion layers (GDL) of polymer electrolyte fuel cells, as depicted in Fig. 12a. At high current density, efficiency is limited by mass transport in the porous layers. The GDL, which is the interconnect between the fluid distributor (bipolar plate) and the catalyst layer, forms the component through which gases, water, heat and electric charge need to transport relevant flux densities. The study of the flow through these layers is important in optimizing fuel cells.

In the current study, 12 GDL sample geometries were obtained. The X-ray scans were acquired during normal operation of the fuel cell. In Fig. 12b, a part of the cathode is visualized. Water, which is a product of reactions in the cathode, is depicted by blue color. Due to the innovative technique used at the SLS beamline, water can be distinguished between the GDL solid material and the air stream. The saturation levels (volume of water compared to the total pore volume) vary at different regions of the GDL. In order to evaluate the permeability dependence on different saturation levels, every GDL is partitioned in three sectors: a) channel region under the air stream channel, b) left rib region and c) right rib region. In total, 12 samples from four GDLs are used to evaluate the material properties. The size of those samples is 1mmX0.6mmX0.16mm (xyz). The details are listed in Table 1, where the dimensions of 12 samples are given in pixels on X, Y and Z direction, respectively; each pixel represents a size of 1.9µm.

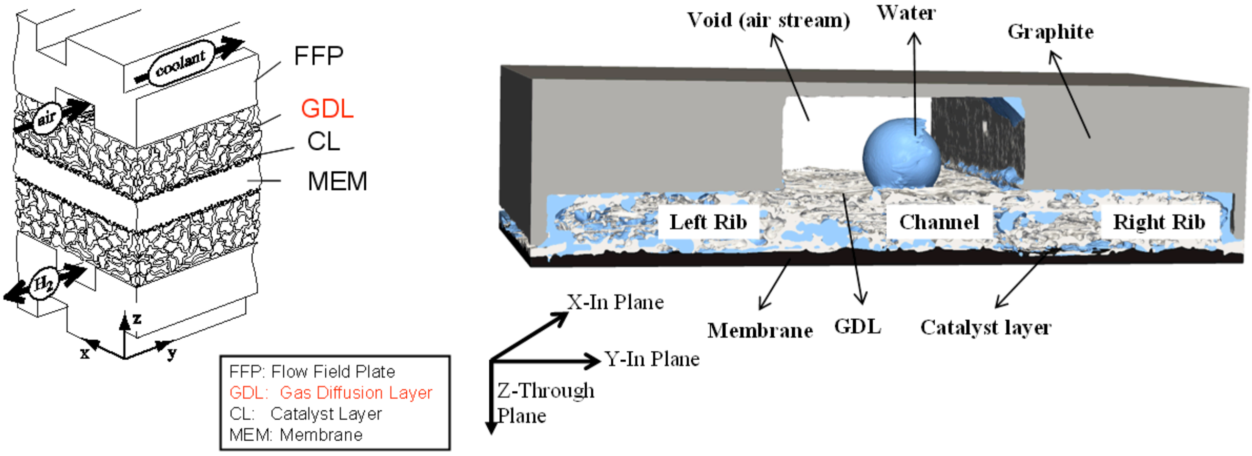

(a) (b)

Figure 12. (a) Schematic of a polymer electrolyte fuel cell system (PEFC); (b) In-situ X-ray images of the cathode of a PEFC (at operating condition).

	Left Rib	Channel	Right Rib
A	$600 \times 340 \times 85$	$600 \times 400 \times 90$	$600 \times 340 \times 85$
Br1	$600 \times 150 \times 80$	$600 \times 400 \times 90$	$600 \times 340 \times 70$
Br2	$600 \times 150 \times 80$	$600 \times 400 \times 90$	$600 \times 340 \times 80$
Br3	$600 \times 150 \times 80$	$600 \times 400 \times 90$	$600 \times 340 \times 80$

Table 1. Dimensions of GDL samples in amount of pixels (of 1.9µm) along each direction. A, Br1, Br2, Br3 are different GDL samples.

The GDL together with the water is depicted in Fig. 13a, giving an overview of the water distribution inside the porous medium. The water phase is displayed in Fig. 13b.

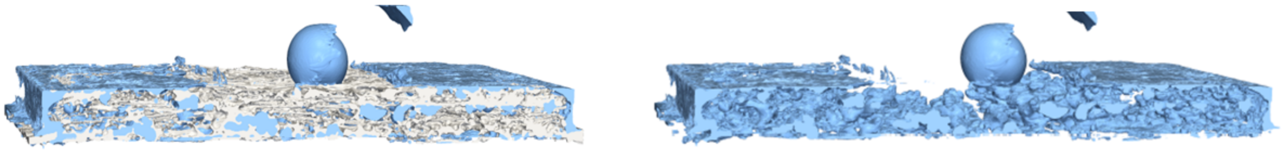

(a) (b)

Figure 13. Rendered solid phase and liquid (water) phase, sample A. (a) GDL and liquid water; (b) liquid water only.

Some interesting and high-valued characteristics that can be obtained, directly after analyzing these pictures are: the porosity, the liquid water saturation and distribution and the local pore diameter distribution. By using the LB method we are able to compute also the permeability and the effective diffusivity, which correspond to the transport properties of the GDL. In order to calculate these transport properties, we compute the flow field as done in the previous section. For instance, for sample A, we examine the dry and wet Left Rib region for the "in-plane" direction (Y-direction, Fig 14a-f).

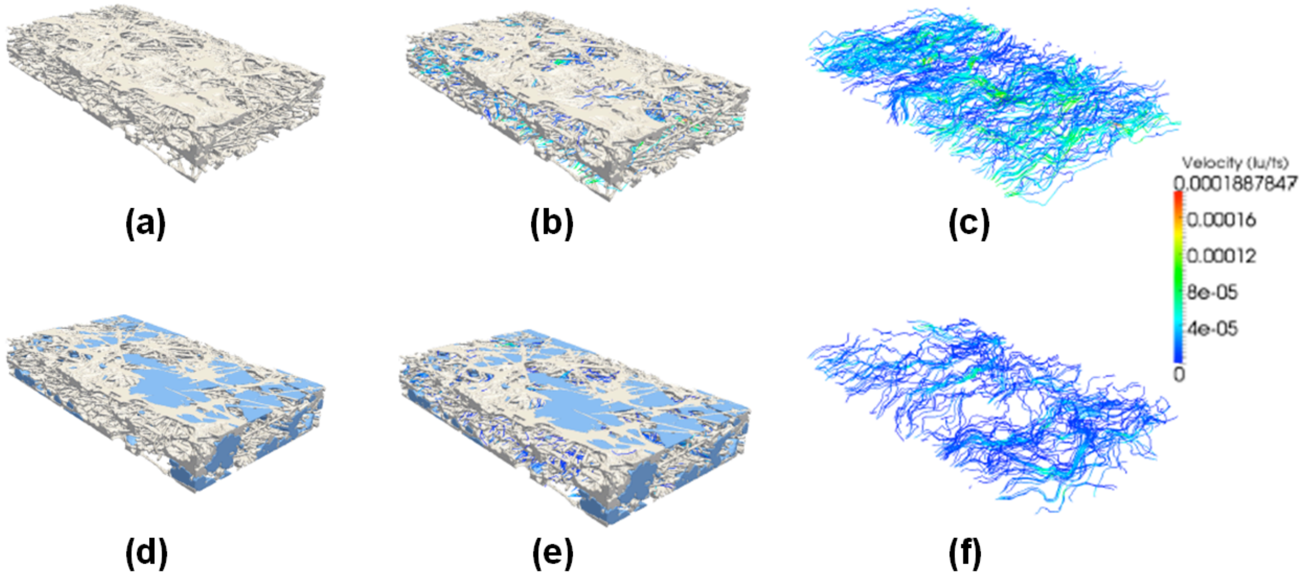

Figure 14. Gas flow through the "Left Rib" domain of Sample A along the "in plane" direction (y-direction). Dry results: (a) domain, (b) domain with streamlines, (c) streamlines. Wet results: (d) domain, (e) domain with streamlines, (f) streamlines.

The permeability can be evaluated as a function of the water saturation. The calculation results are plotted in Fig. 15. Symbols represent the relative permeability (permeability of wet GDL divided by the permeability of dry GDL). The solid line represents the empirical power law, $\kappa_{rg} = (1-S)^{X}$, where X is a fitted parameter. In the literature and more specific in Ref. [19], the value of X was empirically calculated to be X=3 (Fig.15a). To the best of our knowledge, this is the first time that this law is validated, for the case of fuel cell operation.

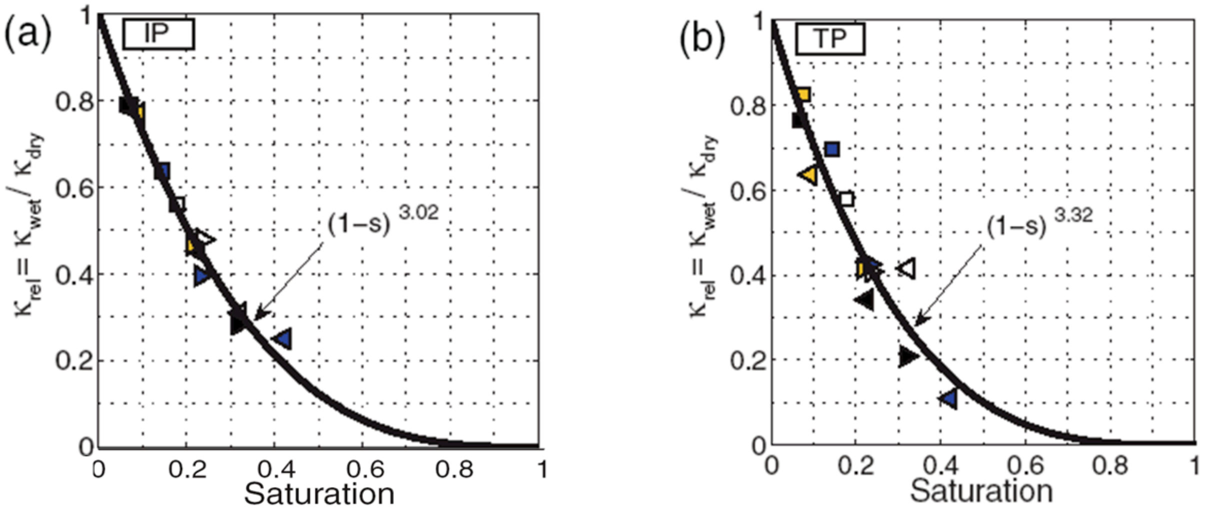

(a) **(b)**

Figure 15. Relative permeability of the different domains (symbols) as a function of saturation; (a) in-plane (IP) and (b) through-plane (TP). 12 samples from 4 GDLs have been used.

The effective diffusivity of the GDL samples has been calculated with two methods. In the first method the LB model is used, while for the second, the GeoDict-DiffuDict module with the explicit jump solver developed by

Wiegmann and Zemitis has been used. For the LB method, the diffusivity was calculated using information of the flowfield and, more specifically, by using the streamlines of single-component flow as presented in Ref. [20]. This methodology was not so accurate and diffusivity results have been calculated in Ref. [21] using the GeoDict software. Simulation results of the normalized effective relative diffusivity versus the saturation are plotted in Fig. 16.

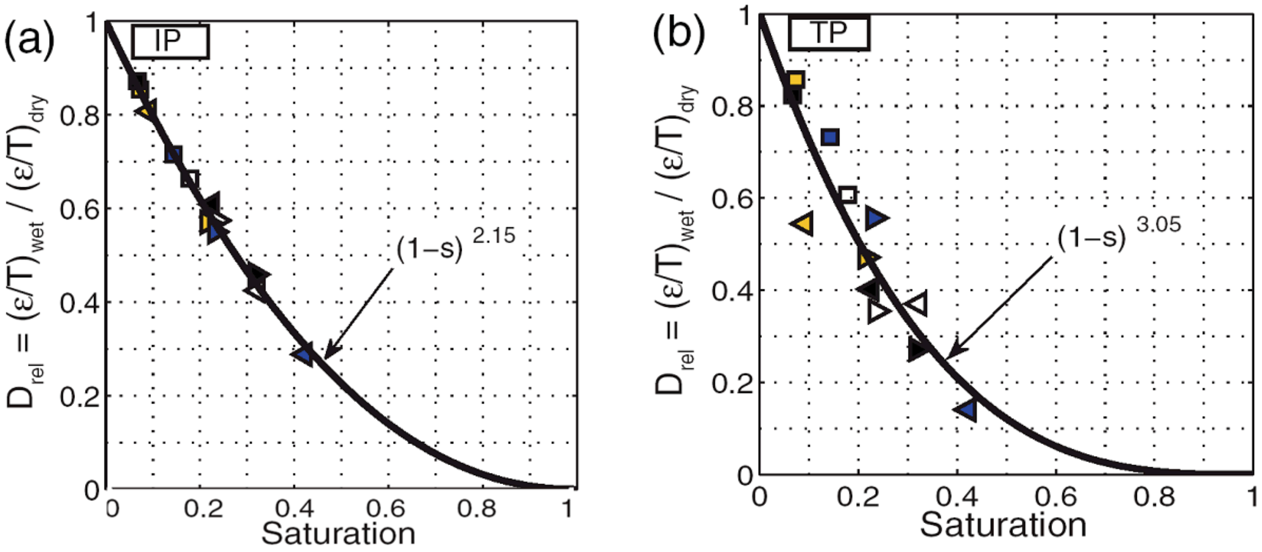

(a) **(b)**

Figure 16. Normalized effective relative diffusivity, D_{rel}, of the different domains as a function of saturation; (a) in-plane (IP), and (b) through-plane (TP).

The simulation results show that both relative permeability and effective relative diffusivity are highly correlated to the GDL saturation. Power law relationships in the form of $(1 - s)^X$ are commonly used in PEFC modeling linking the effective gas transport properties to the saturation of the samples. The present analysis shows that for the saturation-permeability relation an exponent of about 3 is obtained for both in-plane and through-plane directions. The same exponent of 3 is found for the through-plane direction of the saturation-effective relative diffusivity relation, while for the in-plane direction the exponent is about 2, supporting the predictions of Nam and Kaviany [22].

6. Validation of the multicomponent lattice Boltzmann algorithm for complex geometry flows

The recently developed multi-component lattice Boltzmann model (Refs. [6-9]) was validated for complex geometry flows using the commercial CFD software FLUENT. Fluent simulation results have been obtained through the active collaboration with the LTNT-ETHZ group (Professor D. Poulikakos). Lattice Boltzmann (LB) simulations were conducted using the newly developed in-house LB code. The complex geometry domain is a real porous anode of a solid oxide fuel cell (SOFC). It is a digital reconstruction obtained via ion-beam tomography (see Fig. 17). In Fig. 18, the flow through a 2D slice, obtained from the measured 3D geometry is plotted.

A mixture of 70% CH_4 and 30% H_2O, at a temperature of 800 K, enters from the left side of the domain and exits from the right side. Figure 18 provides isocontours of the magnitude of total velocity (left) and y-velocity component (right). Comparison with continuum Navier Stokes CFD simulations using the FLUENT commercial package is also shown in Fig. 18 for a domain size falling in the **macroscopic** regime limit. This can be done by considering a large enough characteristic length-scale of the problem (macroscopic regime: Kn << 1). However, Navier Stokes CFD solvers cannot capture microflow effects and thus provide the same solution, irrespective of the characteristic length of the domain (e.g. 10 cm, or 10 μm).

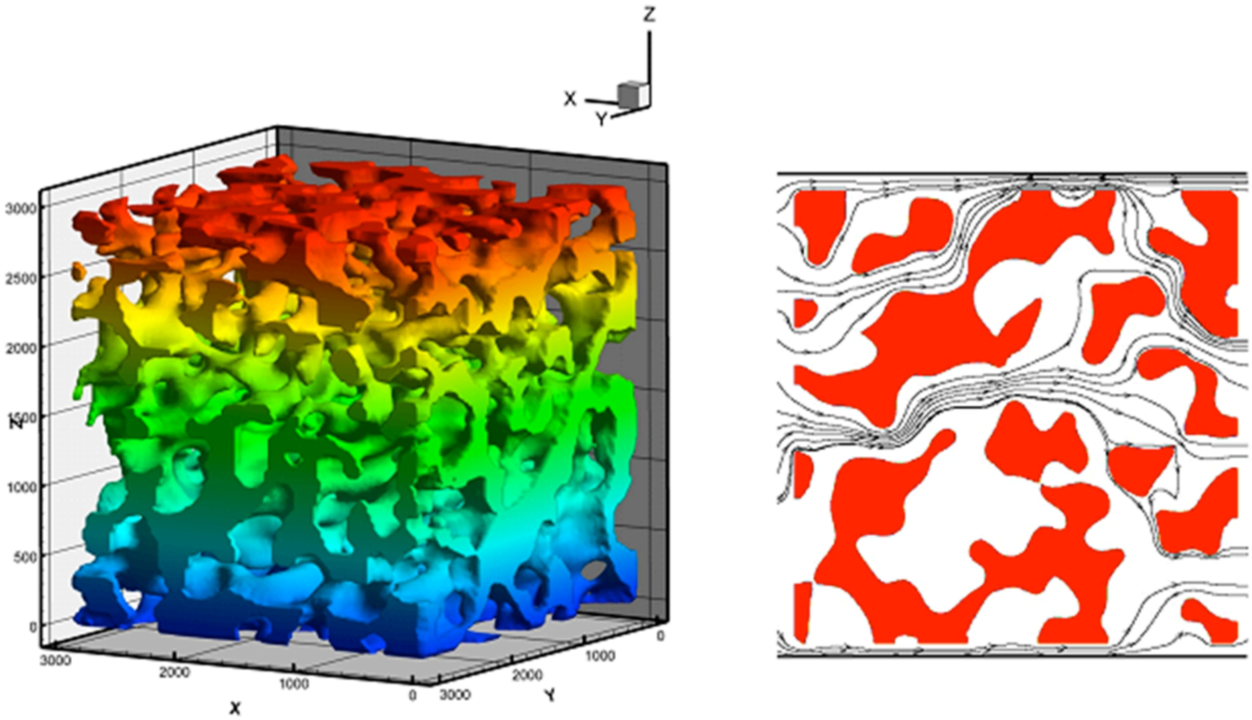

Figure 17: 3D solid oxide anode geometry typically found in solid oxide fuel cells (SOFCs). Geometry provided from EMPA (left). Streamlines of multi-component flow simulations on a 2D slice extracted from the full 3D geometry (right, flow streamlines).

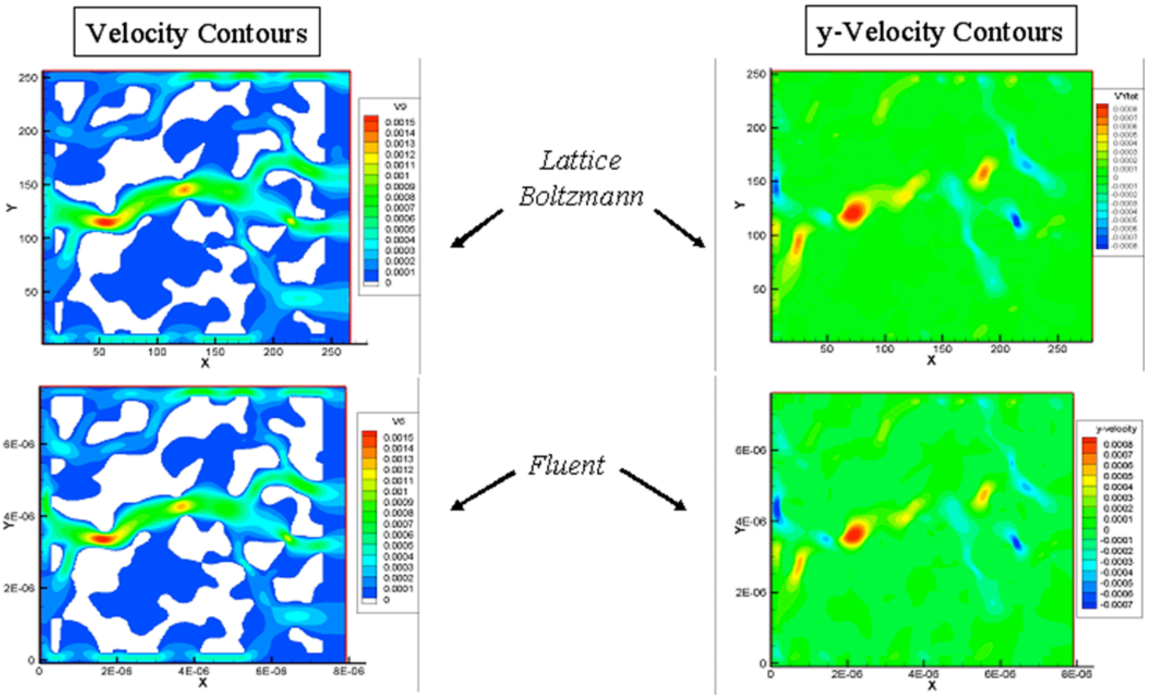

Figure 18. A mixture of CH_4 and H_2O enters from the left side and exits from the right side of the domain. Velocity isocontours (total velocity magnitude left, y-velocity component magnitude right) predictions are compared for LB and a commercial CFD code (Fluent). The color bars provide the velocity magnitude in m/s.

In Fig. 19, a comparison along a specific x-line is shown. The line passes from the location of maximum magnitude of the total velocity. The x- and the y-direction components of the velocity (y-velocity for the FLUENT and VYtot for the LB method) are compared in Fig. 19 (right). The results obtained using two fundamentally different approaches are in excellent agreement at the macroscopic limit. It should be noted that for LB the computational grid is generated instantly, while NS solvers require special grid generation procedures for complex geometries and tuning. This can be extremely advantageous when elaborate parametric studies are needed.

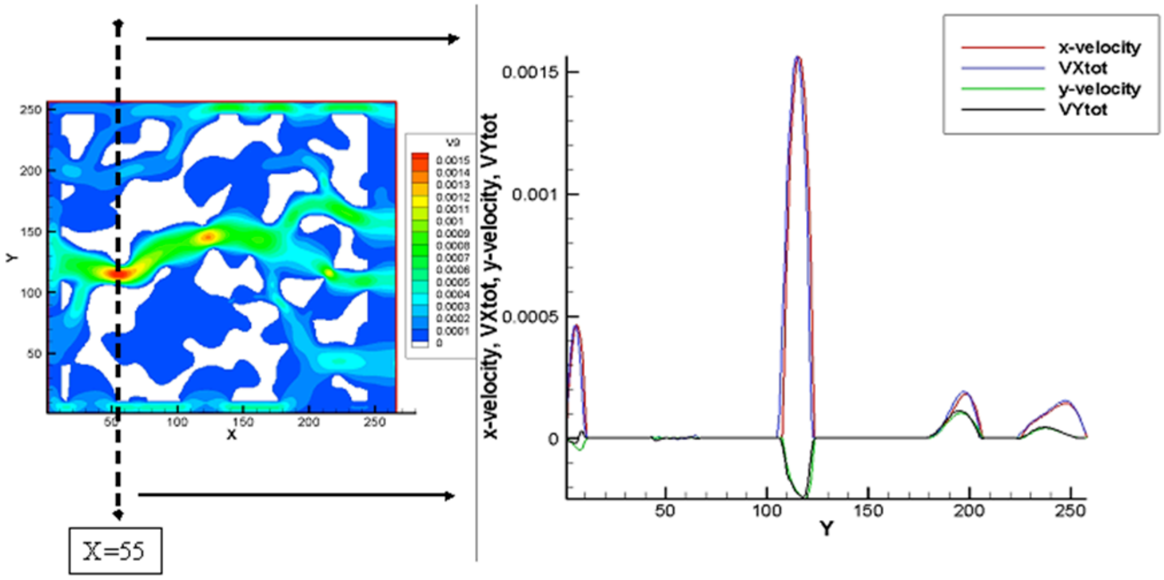

Figure 19. Comparison between FLUENT and lattice Boltzmann predictions along the slice that passes from the location of the maximum mixture velocity (left picture). FLUENT results are denoted with “x-velocity” and “y-velocity”, while Lattice Boltzmann results are marked “VXtot” and “VYtot”. The comparison is performed in the macroscopic regime (Kn << 1). The horizontal axis in the plot to the right denotes the number of computational points. More results can be found in Ref. [23].

7. Transition to micro-flow regime and non-trivial effects

By decreasing the characteristic length scale of the domain, the Knudsen (Kn) number increases and microflow effects, which cannot be described by the standard formulation of NS equations, can be observed. The transition from the macro-world to the micro-world is accompanied by velocity-slip effects. Validation of the method for straight channels was the subject of Refs. [5,6].

Preliminary microflow results for the complex geometry domain seem to be in agreement with the straight channel solutions concerning the amount of slip velocity on the walls. In Fig. 20, the dependence of the maximum velocity achieved throughout the whole computational domain as a function of the characteristic length scale is plotted. The Knudsen number is defined as the ratio of the largest channel gap distance in the computational domain, over the mean free path of the mixture. Due to the emerging slip velocity at the walls, the maximum value of the velocity in the domain decreases in the lattice Boltzmann simulations. This effect cannot be captured by the Navier-Stokes solver, which indicates the same maximum velocity irrespective of the domain physical size.

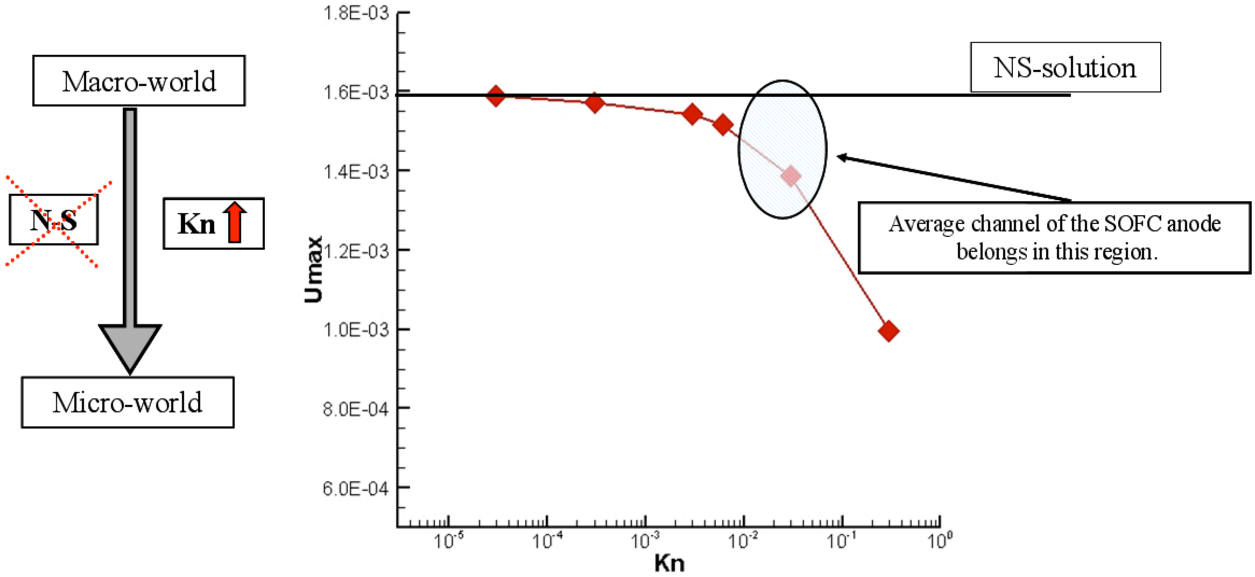

Figure 20. The maximum velocity of the flow in the complex geometry of **Fig. 19** decreases as the Knudsen number of the flow increases. This effect cannot be reproduced by Navier-Stokes macroscopic flow solvers.

8. Summary of achievements– Future Steps

Both targets of the project have been achieved:

a) developing a new mesoscale Lattice Boltzmann model for: multi-species, non-isothermal, reacting, complex three-dimensional geometry flows, and

b) carrying out permeability and diffusivity experiments in a model PEFC.

The main results of the project can be summarized as follows:

- Thermal-multicomponent LB model derivation 2D and 3D, and validations in a large number of benchmark flows.
- Simulation of 3D porous media flows with application to PEFCs.
- Validation of complex geometry algorithm in 2D and 3D against experiments as well as against other CFD numerical tools.
- Study and characterization of the GDL properties, using in-situ X-ray tomography under normal operational conditions (saturation dependent permeability and diffusivity).
- Simulation of bulk chemical reactions.

Collaboration and communication between the Combustion Fundamentals group, the Electrochemistry department and the large facilities of PSI (SLS Beamline) has been established.

In the near future, we are planning:

a) to simulate the flow in domains that describe the full PEFC (Channels + GDL's). This will allow a better understanding of the processes that take place under real operating conditions and will help contribute significantly in the optimization process of the fuel cells.

b) to simulate reacting flows in porous media using the novel thermal-mixture model developed in this project.

9. Distinctions.

1. Our work, received high visibility at the major Lattice Boltzmann confernece that was held this year in India.(21st DSFD Conference) The frontpage of the book of abstracts was covered by the results of our work. Title: N. Prasianakis, T. Rosen, J. Kang, J. Eller, J. Mantzaras, F.N. Buechi, Characterization of saturation-dependent transport properties of gas diffusion layers in PEFCs via 3D flow simulations

2. The master Student, Tomas Rosen received the prize of the best master Thesis of KTH in 2012. Title: Determination of water saturation dependent gas transport properties of PEFC gas diffusion layers via the Lattice Boltzmann method. (Held at PSI)

3. Our work has been a scientific highlight of the energy departement of PSI (ENE) in 2012. Title: Flow modeling in gas diffusion layers of PEFCs at the micro- and mesoscale.

International Collaborations

- Collaboration with KTH, Sweden through the PhD student Tomas Rosen is established.
- Collaboration with University of Torino, Italy with the group of Prof. P. Asinari is established.

Theses

1) Filippo Visconti, **Detailed combustion fields of methane and air mixtures by a model reduction technique,** Master Thesis, Univ. Torino (2011)
2) Tomas Rosen, **Determination of water saturation dependent transport properties of PEFC gas diffusion layers via the Lattice Boltzmann method**, Master Thesis, KTH (2011)

Invited Talks

1. N. Prasianakis, 13 May 2011, U.C. Louvain, Belgium (2011)
2. N. Prasianakis, 2010 annual ERCOFTAC meeting (28 October 2010, ETHZ, Zurich, Switzerland)

Publications

[1] J. Kang, N. Prasianakis, J. Mantzaras, **Lattice Boltzmann model for thermal binary mixture gas flows.** (submitted to Physical Review E, November 2012)

[2] N. Prasianakis, T. Rosen, J. Kang, J. Eller, J. Mantzaras, F.N. Buechi, **Simulation of 3D porous media flows with application to polymer electrolyte fuel cells**, Communications in Computational Physics, 13:851-866, (2013).

[3] A. Di Rienzo, P. Asinari, E. Chiavazzo, N. Prasianakis, J. Mantzaras, **Lattice Boltzmann model for reactive flow simulations**, Europhys. Lett. **98**, 34001 (2012)

[4] T. Rosen, J. Eller, J. Kang, N. Prasianakis, J. Mantzaras, F. N. Büchi, **Saturation dependent effective transport properties of PEFC gas diffusion layers.** J. Electrochem. Soc. **159**, 9, F536 (2012).

[5] N. Prasianakis, S. Ansumali, **Microflow simulations via the lattice Boltzmann method**, *Commun. Comput. Phys.* **9**, 1128 (2011).

[6] N. Prasianakis, J. Mantzaras, **Lattice Boltzmann modeling for energy conversion systems,** 63rd meeting of DFD of APS, Vol. 55 (16), p. 352, 2010.

[7] N.Prasianakis, J. Mantzaras, I. Zinovik, D. Poulikakos, **Microflow simulation in porous media components of fuel cell systems** (draft/under preparation).

Conference presentations/ proceedings

1) N. Prasianakis, T. Rosen, J. Kang, J. Eller, J. Mantzaras, F.N. Buechi, Characterization of saturation-dependent transport properties of gas diffusion layers in PEFCs via 3D flow simulations, 21th International Conference on Discrete Simulation of Fluid Dynamics, Bangalore, India (2012)
2) J. Kang, N. Prasianakis, J. Mantzaras, Development of an LB model for non-isothermal mixture flows, 21th International Conference on Discrete Simulation of Fluid Dynamics, Bangalore, India (2012)
3) J. Eller, T. Rosén, N.I. Prasianakis, J. Kang, J. Mantzaras, J. Roth, F. Marone, M. Stampanoni, A. Wokaun, F.N. Büchi, Insight into the 3D Water Distribution in PEFC Gas Diffusion Layer by In-situ X-ray Tomographic Microscopy, 9th Symposium on Fuel Cell and Battery Modeling and Experimental Validation (ModVal 9), CAMPUS Sursee, Switzerland, April 2–4, (2012)
4) N.Prasianakis, J.Kang, J.Mantzaras, Lattice Boltzmann approaches for thermal multi-component flows in complex geometries, 8th ICMMES conference, Lyon, France (2011)
5) F. Di Rienzo, P. Asinari, E. Chiavazzo, N. I. Prasianakis, J. Mantzaras, A Lattice Boltzmann model for reactive flows simulation,13th International Conference on Numerical Combustion, Greece, (2011)
6) F. Di Rienzo, P. Asinari, E. Chiavazzo, N. I. Prasianakis, J. Mantzaras, Coupling Lattice Boltzmann with Reduced Chemical Kinetics for Combustion Simulations, 8th ICMMES conference, Lyon, France (2011)
7) J.Kang, N.Prasianakis, J. Mantzaras, Lattice Boltzmann method for thermal multi-component flow simulation on standard lattices with application to energy conversion systems, 20th International Conference on Discrete Simulation of Fluid Dynamics, North Dakota, USA (2011)
8) T. Rosen, N. Prasianakis, J. Kang, J. Eller, J. Mantzaras, F.N. Buechi, In-situ measurements of gas transport properties in gas diffusion layers of PEFCs, Tagung Verbrennungsforschung in der Schweiz, ETH Zürich, Switzerland (2011)
9) N. Prasianakis, J. Kang, F. N. Büechi, J. Mantzaras, Modeling of heat transfer and mixing processes for complex geometries with applications to energy conversion systems, 64th Annual meeting of the American Physical Society, division of fluid dynamics, Baltimore, USA (2011)
10) N. Prasianakis et al. , 19th Discrete Simulation of Fluid Dynamics (DSFD 2010, July 2010, Rome, Italy)
11) N. Prasianakis et al. , Transpore 2010 Conference (19-20 August 2010, PSI Switzerland)
12) N. Prasianakis et al. , 63rd annual meeting of the American Physical Society APS, Division of fluid dynamics (23rd November 2010, Long Beach, USA)
13) N. Prasianakis et al. , 4th Swiss lattice Boltzmann meeting (December 2009, Zurich, Switzerland).
14) Verbrennungforschung in der Schweiz (28th October 2009, ETH Zurich)
15) N. Prasianakis et al. , 1st International Conference on computational methods for thermal problems (Sept. 2009, Napoli, Italy).

Conference organization

- 4th Swiss lattice Boltzmann meeting (December 2009, Zurich, Switzerland). More than 50 participants from major European institutions.

Personnel planning

- A PhD student joined the Combustion Fundamentals Group (CFG) to work in the project on 1 February 2010 (Ms. Jinfen Kang).
- A PhD student, Mr. Antonio-Fabio Di Rienzo, from University of Torino, working in the area of Lattice Boltzmann modeling under the supervision of Prof. Asinari, spent 3 months at the CFG group starting (23 August to 23 November, 2010. This exchange student fostered our international co-operations.
- A Master student, Mr. Tomas Rosen from KTH, Stockholm, Sweden stayed at PSI (working for both the CFG and LEC groups) for 6 months starting 5 January 2011. His main tasks were to obtain the “wet” X-ray tomography data of Polymer Electolyte Fuel Cell (PEMC) diffusion layers and to work on the development of the 3D lattice Boltzmann algorithm.
- A Master student, Mr. Filippo Visconti from from University of Torino, working in the area of Lattice Boltzmann modeling under the supervision of Prof. Asinari, spent 2 months at the CFG group starting (February-March) 2010. This exchange student was a follow-up of Mr Di Rienzo work.

10. References

1. N.I. Prasianakis and I. Karlin, **Lattice Boltzmann simulation of thermal flows on standard lattices**, Phys. Rev. E **76**, 016702 (2007).
2. N.I. Prasianakis and I. Karlin, **Lattice Boltzmann method for compressible flows on standard lattices**, Phys. Rev. E **78**, 016704 (2008).
3. N.I. Prasianakis, I.V. Karlin, J. Mantzaras and K.B. Boulouchos, **Lattice Boltzmann method with restored Galilean invariance**, Phys. Rev. E **79**, 066702 (2009).
4. N.I. Prasianakis and K.B. Boulouchos, **Lattice Boltzmann method for simulation of weakly compressible flows at arbitrary Prandtl number**, Int. J. Mod. Phys. C **18**, 602 (2007).
5. S. Ansumali, I. Karlin, S. Arcidiacono, A. Abbas and N.I. Prasianakis, **Hydrodynamics beyond Navier-Stokes: Exact solution to the lattice Boltzmann hierarchy**, Phys. Rev. Lett. 98, 124502 (2007).
6. S. Arcidiacono, J. Mantzaras, I.V. Karlin, Lattice **Boltzmann modeling of catalytic reactions**, Phys. Rev. E 78, 046711 (2008)
7. S. Arcidiacono, I.V. Karlin, J. Mantzaras, and C. Frouzakis, **Lattice Boltzmann Model for the Simulation of Multicomponent Mixtures**, Phys. Rev. E 76, 046703 (2007)
8. S. Arcidiacono, J. Mantzaras, S. Ansumali, I.V. Karlin, C. Frouzakis, K. Boulouchos, **Simulation of binary mixtures with the Lattice Boltzmann method**, Phys. Rev. E, 74, 056707, (2006).
9. S. Arcidiacono, S. Ansumali, I.V. Karlin, J. Mantzaras, K. Boulouchos, **Entropic lattice Boltzmann method for simulation of binary mixtures**, *Mathematics and Computers in Simulation*, 72, 79-83, (2006).
10. J. Kang, N. Prasianakis, J. Mantzaras, **Lattice Boltzmann model for thermal binary mixture gas flows**. (submitted to Physical Review E, November 2012)
11. Andrew E. Lutz, Robert J. Kee, Joseph F. Grcar, Fran M. Rupley, **OPPDIF: A FORTRAN PROGRAM FOR COMPUTING OPPOSED-FLOW DIFFUSION FLAMES**, Sandia National Laboratories,Livermore, USA, SAND96-8243, Unlimited Release, (1997)
12. A. Di Rienzo, P. Asinari, E. Chiavazzo, N. Prasianakis, J. Mantzaras, **Lattice Boltzmann model for reactive flow simulations**, Europhys. Lett. **98**, 34001 (2012)
13. Fluent Inc., **FLUENT**, Release 6. 3, User Guide (Fluent Inc.) 2006.
14. Pizza G., Frouzakis C. E., Mantzaras J., Tomboulides A. G. and Boulouchos K., Combust. Flame, **155** (2008).
15. J. Li, Z. Zhao, A. Kazakov, F. L. Dryer, **An updated comprehensive kinetic model of hydrogen combustion,** Int. J. Chem. Kinet. **36**, 566 - 575 (2004)
16. Marinov N. M., Westbrook C. K. and Pitz W. J., **Detailed and Global Chemical Kinetic Model for Hydrogen**, Transport Phenomena in Combustion, Vol. 1 (Taylor and Francis, Washington DC, 1996)
17. X. He, Q. Zou, L.Luo and M. Dembo, **Analytic solution of simple flows and analysis of nonslip boundary conditions for the lattice Boltzmann BGK model,** J. Stat. Phys. 87, 115-136 (1997)
18. S. Ansumali and I. Karlin, **Kinetic boundary condition for the lattice Boltzmann method**, Phys. Rev. E 66, 026311 (2002).
19. S. Litster and N. Djilali, “**Transport Phenomena In Fuel Cells**” 175~213, (2005).
20. N. Prasianakis, T. Rosen, J. Kang, J. Eller, J. Mantzaras, F.N. Buechi, **Simulation of 3D porous media flows with application to polymer electrolyte fuel cells**, Communications in Computational Physics, 13:851-866, (2013).
21. T. Rosen, J. Eller, J. Kang, N. Prasianakis, J. Mantzaras, F. N. Büchi, **Saturation dependent effective transport properties of PEFC gas diffusion layers**, J. Electrochem. Soc. 159, 9, F536 (2012).
22. J. H. Nam and M. Kaviany, **Effective diffusivity and water-saturation distribution in single- and two-layer PEMFC diffusion medium**, Int. J. Heat Mass Transfer, **46**, 4595 (2003).
23. N.Prasianakis, J. Mantzaras, I. Zinovik, D. Poulikakos, **Microflow simulation in porous media components of fuel cell systems** (draft available 2012).

11 Appendix: Thermal mixture description

Thermal binary-mixture model

A binary gas mixture, which is composed of two species *A*, *B* is under consideration. Each species of the gas mixture is represented by one particle distribution function f_j where in this example j=A,B. Each species obeys its own BGK-type kinetic equation which can be expressed as:

$$\partial_t f_{ji} + c_{ji\alpha}\partial_\alpha f_{ji} = -\frac{1}{\tau_1}\left(f_{ji} - f^*_{ji}\right) - \frac{1}{\tau_2}\left(f^*_{ji} - f^{eq}_{ji}\right) + \psi_{ji} + \phi_{ji} \quad (1)$$

Where i=0,…N, is the number of discrete velocities $c_{ji\alpha}$, and α={x,y,z}. The current study is based on the standard D2Q9 lattice where N=9 and α={x,y}. Therefore the set of discrete velocities can be written as:

$$c_{jix} = c_j\left\{0,1,0,-1,0,1,-1,-1,1\right\}$$

$$c_{jiy} = c_j\left\{0,0,1,0,-1,1,1,-1,-1\right\},$$

with c_j being a velocity related to the speed of sound. The terms $\boldsymbol{\psi}_{\mathbf{ji}}$ are responsible for the momentum equation, while the terms $\boldsymbol{\varphi}_{\mathbf{ji}}$ deliver exact energy equation and allow the control of the Prandtl number. The BGK relaxation process is split in two parts following the quasi-equilibrium (QE). The first part is characterized by a fast-relaxation process toward an intermediate state, represented by f^*_{ji}, while the second part describes a slow-relaxation process toward the thermodynamic equilibrium, represented by f^{eq}_{ji}. The relevant moments for each species are the following:

$$\rho_j = \sum_{i=0}^{8} f_{ji}\,,\ J_{j\alpha} = \sum_{i=0}^{8} f_{ji}c_{ji}\,,\ E_j = \sum_{i=0}^{8} f_{ji}c_j^2$$

$$P_{j\alpha\beta} = \sum_{i=0}^{8} f_{ji}c_{ji\alpha}c_{ji\beta}\ ,\ Q_{j\alpha\beta\gamma} = \sum_{i=0}^{8} f_{ji}c_{ji\alpha}c_{ji\beta}c_{ji\gamma}$$

$$q_{j\alpha} = \sum_{i=0}^{8} f_{ji}c_{ji\alpha}c_{ji}^2\ ,\ R_{\alpha\beta} = \sum_{i=0}^{8} f_{ji}c_{ji\alpha}c_{ji\beta}c_{ji}^2$$

namely the density, momentum, energy, pressure tensor, third order moment, third order contracted moment, and fourth order contracted moments.

Equilibrium distribution functions

The equilibrium distribution function f^{eq}_{ji} is calculated as minimizers of the H-function,

$$H = \sum_{j}^{A,B}\sum_{i=0}^{8} f_{ji}\ln f_{ji},$$

under specific constraints. The constraints applied in this case are the species density ρ_j, the momentum of the mixture J_α and the energy of the mixture E:

$$\sum_{i=0}^{8} f^{eq}_{ji} = \rho_j\ ,\ \sum_{j}^{A,B}\sum_{i=0}^{8} f^{eq}_{ji}c_{ji\alpha} = J^{eq}_\alpha = J_{A\alpha} + J_{B\alpha}\,,$$

$$\sum_{j}^{A,B}\sum_{i=0}^{8} f^{eq}_{ji}c_{ji}^2 = \sum_{j}^{A,B}\sum_{i=0}^{8} f_{ji}c_{ji}^2 = 2CT + \frac{J^2}{\rho} = E_A + E_B\,,$$

where T is the temperature of the mixture, and C is the total concentration of the mixture defined as

$$C = \sum_{j}^{A,B} C_j = \sum_{j}^{A,B} \rho_j / M_j$$

where M_j is the molar mass of component j. An additional constraint is introduced in order to increase the accuracy of the higher order moment similar to the guided-equilibrium populations of the single component thermal model:

$$P^{eq}_{\alpha\beta} = \sum_{j}^{A,B}\sum_{i=0}^{8} f^{eq}_{ji}c_{ji\alpha}c_{ji\beta} = CT\delta_{\alpha\beta} + \frac{J_\alpha J_\beta}{\rho},$$

$$P^{eq}_{A\alpha\beta} = C_A T\delta_{\alpha\beta} + \rho_A\frac{J_\alpha J_\beta}{\rho^2}\,,\ P^{eq}_{B\alpha\beta} = C_B T\delta_{\alpha\beta} + \rho_B\frac{J_\alpha J_\beta}{\rho^2}$$

The result of the minimization produces the equilibrium populations which takes the following form for each species:

$$f_{ji}^{eq}(\rho_j,u_\alpha,T)=\rho_j\prod_{\alpha=x,y}\frac{\left(1-2c_{ji\alpha}^2\right)}{2^{C_{ji\alpha}^2}}\left[\left(c_{ji\alpha}^2-1\right)+c_{ji\alpha}u_\alpha+u_\alpha^2+\frac{T}{M_j}\right]$$

where u_α is the velocity of the mixture defined as $u_\alpha = J_\alpha /\rho$. The auxiliary state f^* is derived by minimizing the H-functional under different constraints. The constraint of total momentum conservation is replaced by the individual momentum conservation,

$$J_{j\alpha}^*=\sum_{i=0}^{8}f_{ji}^*c_{ji\alpha}=\sum_{i=0}^{8}f_{ji}c_{ji\alpha}=J_{j\alpha},$$

and the result of the minimization is quite similar to the equilibrium distribution function and reads:

$$f_{ji}^*(\rho_j,u_{j\alpha},T)=\rho_j\prod_{\alpha=x,y}\frac{\left(1-2c_{ji\alpha}^2\right)}{\left(2\right)^{C_{ji\alpha}^2}}\left[\left(c_{ji\alpha}^2-1\right)+c_{ji\alpha}u_{j\alpha}+u_{j\alpha}^2+\frac{T}{M_j}\right]$$

where $u_{j\alpha}$ is the velocity of species j, defined as $u_{j\alpha} = J_{j\alpha} /\rho$. Using the aforementioned distribution functions, it is possible to study the macroscopic thermo-hydro-dynamic limit.

Deviation Terms

The moments of the equilibrium distribution function are in agreement with the ones predicted in the Kinetic theory of gases (Maxwell Boltzmann form (MB)) up to the second order. The higher order moments are:

$$P_{j\alpha\beta}^{eq}=P_{j\alpha\beta}^{MB}=C_jRT\delta_{\alpha\beta}+\rho_j\frac{J_\alpha J_\beta}{\rho^2}$$

$$Q_{j\alpha\beta\gamma}^{eq}=Q_{j\alpha\beta\gamma}^{MB}+Q'_{j\alpha\beta\gamma}=C_jRT(\frac{J_\alpha}{\rho}\delta_{\beta\gamma}+\frac{J_\beta}{\rho}\delta_{\alpha\gamma}+\frac{J_\gamma}{\rho}\delta_{\alpha\beta})+\rho_j\frac{J_\alpha J_\beta J_\gamma}{\rho^3}+Q'_{j\alpha\beta\gamma}$$

$$q_{j\alpha}^{eq}=q_{j\alpha}^{MB}+q'_{j\alpha}=\rho_j\frac{J_\alpha}{\rho}\left(\frac{J^2}{\rho^2}+\frac{4RT}{M_j}\right)+q'_{j\alpha}$$

$$R_{j\alpha\beta}^{eq}=R_{j\alpha\beta}^{MB}+R'_{j\alpha\beta}=C_jRT\left(\frac{J^2}{\rho^2}+\frac{4RT}{M_j}\right)\delta_{\alpha\beta}+\rho_j\frac{J_\alpha J_\beta}{\rho^2}\left(\frac{6RT}{M_j}+\frac{J^2}{\rho^2}\right)+R'_{j\alpha\beta}$$

where $Q'_{j\alpha\beta\gamma}$, $q'_{j\alpha}$ and $R'_{j\alpha\beta}$ are the deviations of the equilibrium higher order moments from MB form. These deviations are known exactly:

$$Q'_{j\alpha\beta\gamma}=\rho\left[-\frac{J_\alpha^3}{\rho^3}+\frac{J_\alpha}{\rho}\left(1-3\frac{RT}{M_j}\right)\right]\delta_{\alpha\beta}\delta_{\alpha\gamma}\delta_{\beta\gamma}$$

$$q'_{j\alpha}=\rho_j\frac{J_\alpha}{\rho}\left(1-3\frac{RT}{M_j}\right)-\rho_j\frac{J_\alpha^3}{\rho^3}$$

$$R'_{j\alpha\beta}=\rho_j\left(\frac{RT}{M_j}-3\frac{R^2T^2}{M_j^2}-\frac{J_\alpha J_\beta}{\rho^2}+\frac{J_\alpha^3J_\beta}{\rho^4}\right)\delta_{\alpha\beta}+\rho_j\frac{J_\alpha J_\beta}{\rho^2}\left[2-6\frac{RT}{M_j}-\frac{J_\alpha^2}{\rho^2}-\frac{J_\beta^2}{\rho^2}\right]$$

The effect of this deviation at the macroscopic limit can be calculated via the Chapman Enskog asymptotic analysis and further neutralized by the proper introduction of counter-terms at the level of the lattice BGK equation.

Diffusivity, Schmidt number

The model recovers the Maxwell-Stefan diffusion equation as:

$$\partial_\alpha X_A=\frac{X_AX_B}{D_{AB}}\left(\frac{J_{B\alpha}}{\rho_B}-\frac{J_{A\alpha}}{\rho_A}\right)+\left(Y_A-X_A\right)\frac{\partial_\alpha P}{P},$$

with X_j beeing the mole fraction of species j, $X_j=C_j/C$, and Y_j is the mass fraction. The mass diffusivity D_{AB} is equal to

$$D_{AB} = \frac{\tau_2 X_A X_B P}{m_{AB}},$$

With $m_{AB}=\rho_A\rho_B/\rho$ being the reduced mass. The Schmidt number of the mixture is a controllable parameter and for the current model is finally defined as:

$$Sc = \frac{\mu}{D_{AB}\rho} = \frac{Y_A Y_B}{X_A X_B}\frac{\tau_1}{\tau_2}$$

Momentum equation, viscosity

The momentum equation reads:

$$\partial_t J_\alpha + \partial_\alpha P + \partial_\beta \left[\frac{j_\alpha j_\beta}{\rho} - \mu \partial_\gamma \left(\frac{J_\alpha}{\rho}\delta_{\beta\gamma} + \frac{J_\beta}{\rho}\delta_{\alpha\gamma} - \frac{J_\gamma}{\rho}\delta_{\alpha\beta} \right) \right] + \partial_\beta P''_{\alpha\beta} = 0.$$

Here, $P''_{\alpha\beta}$ is the representation of the deviation of the current model's momentum equation compared to the Navier-Stokes momentum equation. In this expression, the pressure is depicted as $P=CT$, the dynamic viscosity is identified as $\mu=\tau_1 CT$. The deviation terms induced by each species to the momentum equation on X and Y direction are:

$$\partial_\beta P''_{jx\beta} = -\partial_x \left\{ \begin{matrix} \tau_1 \partial_x \left[\rho_j \frac{J_x}{\rho}\left(1 - 3\frac{T}{M_j}\right) - \rho_j \frac{J_x^3}{\rho^3} \right] \\ -\tau_1 \frac{X_j}{2}\left[\partial_x \left(J_x - 3\frac{J_x}{M}T - \frac{J_x^3}{\rho^2} \right) + \partial_y \left(J_y - 3\frac{J_y}{M}T - \frac{J_y^3}{\rho^2} \right) \right] \end{matrix} \right\}$$

$$\partial_\beta P''_{jy\beta} = -\partial_y \left\{ \begin{matrix} \tau_1 \partial_y \left[\rho_j \frac{J_y}{\rho}\left(1 - 3\frac{T}{M_j}\right) - \rho_j \frac{J_y^3}{\rho^3} \right] \\ -\tau_1 \frac{X_j}{2}\left[\partial_x \left(J_x - 3\frac{J_x}{M}T - \frac{J_x^3}{\rho^2} \right) + \partial_y \left(J_y - 3\frac{J_y}{M}T - \frac{J_y^3}{\rho^2} \right) \right] \end{matrix} \right\}$$

and by summing up for different species we obtain the total value for the mixture $\partial_\beta P''_{\alpha\beta} = \partial_\beta P''_{A\alpha\beta} + \partial_\beta P''_{B\alpha\beta}$.

By knowing the exact form of the deviation, the correction terms take the following form: $\psi_{ji} = \Psi_{j\alpha}\partial_\kappa P''_{\alpha\kappa}$.

Energy equation, thermal conductiviy

The equation which describes the evolution of temperature is identified as:

$$\partial_t T = -u_\alpha \partial_\alpha T - T\partial_\alpha u_\alpha + \frac{1}{C}\partial_\alpha \left(\kappa \partial_\alpha T \right) - \frac{2}{C}\partial_\alpha \left(T \sum_j \frac{V_{j\alpha}}{M_j} \right)$$

$$
\begin{aligned}
&+\frac{\mu}{C}\partial_\alpha u_\beta\left(\partial_\alpha u_\beta+\partial_\beta u_\alpha-\partial_\gamma u_\gamma\delta_{\beta\alpha}\right)\\
&-\frac{1}{2C}\left(\partial_\alpha q'_\alpha+\partial_\alpha q''_\alpha\right)
\end{aligned}
\tag{1}
$$

In this expression, $\boldsymbol{\kappa}$ is the thermal conductivity of the model which is equal to:

$$\kappa = 2\tau_1 CT\sum_{j}^{A,B}\frac{X_j}{M_j}$$

The fourth term in the right hand side of Eq. (1) is the enthalpy flux relative to the average motion of the mixture. It accounts for energy changes due to composition changes, that occur during species diffusion. It prevents local violations of the entropy condition. More specific, in combustion applications, omission of this term can generate spurious temperature gradients. This in turn, can incorrectly initiate the combustion of the mixture.

The last term of Eq. (1) represents the deviation of the current bare model from the continuum energy equation. Knowing its exact analytic form allows us to design in a proper way the applied correction scheme. The deviation term of energy equation contains $\partial_\alpha q'_\alpha$ and $\partial_\alpha q''_\alpha$. The former is already known, the expression of latter is found to be, $\partial_\alpha q''_\alpha = \partial_\alpha q''_{A\alpha} + \partial_\alpha q''_{B\alpha}$, where:

$$
\begin{aligned}
q''_{j\alpha} &= +3\tau_1 CR^2T\frac{X_j}{M_j}\partial_\alpha T\\
&+\tau_2\left(1-3\frac{RT}{M_j}\right)\left[Y_j\partial_\alpha P-\partial_\alpha\left(X_jP\right)\right]+\dots\\
&\left\{
\begin{aligned}
&+\tau_1\left[\begin{aligned}&\frac{3X_jJ_\alpha J_\gamma}{2\rho}R\partial_\gamma\frac{T}{M}-\frac{3X_jPJ_\alpha}{\rho}\partial_\gamma\frac{J_\gamma}{\rho}-\frac{3Y_jJ_\alpha^2}{\rho^2}\partial_\alpha P+3X_j\frac{J_\alpha J_\gamma}{\rho^2}\frac{CRT}{M}\partial_\gamma M\\
&+\left(\frac{J^2}{\rho^2}\delta_{\alpha\beta}+2\frac{J_\alpha J_\beta}{\rho^2}\right)\left[Y_j\partial_\beta P-\partial_\beta\left(X_jP\right)\right]+\partial_\alpha\frac{Y_jJ_\alpha^2}{\rho}\end{aligned}\right]\\
&+\tau_1\left[-\left(1-3\frac{RT}{M_A}\right)\partial_\gamma\left(Y_A\frac{J_\alpha J_\gamma}{\rho}\right)+\frac{X_A}{2}\left(1-3R\frac{T}{M}\right)\frac{J_\alpha}{\rho}\partial_\gamma j_\gamma\right]\\
&+\tau_1\left[-\partial_\beta\left(Y_A\frac{J_\alpha^3J_\beta}{\rho^3}\right)-\frac{X_A}{2}\frac{J_\alpha}{\rho}\partial_\gamma\frac{J_\gamma^3}{\rho^2}-\partial_\alpha\frac{Y_jJ_\alpha^4}{\rho^3}+\partial_\beta\left(\frac{Y_jJ_\alpha^3J_\beta}{\rho^3}+\frac{Y_jJ_\alpha J_\beta^3}{\rho^3}\right)\right]
\end{aligned}
\right\}\textbf{can be neglected in standard applications}
\end{aligned}
$$

The final form of the correction terms for the energy equation is: $\phi_{ji} = \Phi_i\partial_\alpha\left(q'_{j\alpha}+q''_{j\alpha}\right)$